



**HAL**  
open science

## Pore pressure behavior in undrained triaxial shear tests on joints

G Archambault, S Poirier, A Rouleau, Sylvie Gentier

► **To cite this version:**

G Archambault, S Poirier, A Rouleau, Sylvie Gentier. Pore pressure behavior in undrained triaxial shear tests on joints. Société Internationale de Mécanique des Roches / International Society for Rock Mechanics / Internationale Gesellschaft für Felsmechanik. 9<sup>e</sup> Congrès International de Mécanique des Roches : Compte-rendus / 9th International Congress on Rock Mechanics: Proceedings / 9 International Kongress über Felsmechanik : Berichte, pp.741-745, 1999. hal-03740047

**HAL Id: hal-03740047**

**<https://brgm.hal.science/hal-03740047>**

Submitted on 28 Jul 2022

**HAL** is a multi-disciplinary open access archive for the deposit and dissemination of scientific research documents, whether they are published or not. The documents may come from teaching and research institutions in France or abroad, or from public or private research centers.

L'archive ouverte pluridisciplinaire **HAL**, est destinée au dépôt et à la diffusion de documents scientifiques de niveau recherche, publiés ou non, émanant des établissements d'enseignement et de recherche français ou étrangers, des laboratoires publics ou privés.

**SOCIETE INTERNATIONALE  
DE MECANIQUE DES ROCHES**

**INTERNATIONAL SOCIETY  
FOR ROCK MECHANICS**

**INTERNATIONALE GESELLSCHAFT  
FÜR FELSMCHANIK**



**Congrès International  
de Mécanique des Roches**

**International Congress on  
Rock Mechanics**

**Internationaler Kongress  
über Felsmechanik**

**COMPTES-RENDUS / PROCEEDINGS / BERICHTE**

OFFPRINT

**Editeurs / Editors / Herausgeber  
G.VOUILLE & P. BEREST**



**Paris / France / 1999**

# Pore pressure behavior in undrained triaxial shear tests on joints

Comportement de la pression interstitielle dans des essais de cisaillement triaxiaux non drainés sur des joints

Porendruckverhalten beim nicht entwässertem Triaxialscherversuch auf Klüften

G.ARCHAMBAULT, S. POIRIER & A. ROULEAU, CERM, Université du Québec, Chicoutimi, Que., Canada

S.GENTIER, BRGM, Direction de la Recherche, Orléans, France

J. RISS, Centre de Développement des Géosciences Appliquées, Université de Bordeaux, France

**ABSTRACT :** In jointed samples the application of a deviatoric stress initially produced an increasing phase of pore pressure during the friction mobilization phase, followed by the roughness mobilization corresponding to the beginning of a progressive decrease of pore pressure. The increase and decrease in pore pressure is different from one sample to the other mainly due to the influence exerted by the roughness morphology. Stress paths were defined for both intact and jointed specimens, controlled by initial effective confining pressure, differential stress and maximum induced pore pressure in the first case, while in the latter the controlling factors were the effective normal stress and the roughness morphology on the joint surfaces.

**RÉSUMÉ :** Dans les échantillons fracturés, l'application d'une contrainte déviatorique produit initialement un accroissement de la pression interstitielle durant la phase de mobilisation du frottement, suivi par la mobilisation de la rugosité, correspondant au début d'une décroissance progressive de la pression interstitielle. La croissance et la décroissance de la pression interstitielle est différente d'un échantillon à l'autre dû principalement à l'influence exercée par la morphologie des épontes de chaque fracture. Les trajectoires des contraintes ont été définies pour les éprouvettes intactes et fracturées, contrôlées par la pression de confinement effective initiale, le différentiel des contraintes et la pression interstitielle induite maximale dans le premier cas tandis que dans le second cas les facteurs de contrôle sont la contrainte normale effective et la morphologie des épontes du joint.

**ZUSAMENFASSUNG :** Die Ausführung eines deviatorischen Streßes an klüftigen Bausteine erzeugt anfangs eine zunehmende Porendrucksphase während der Frictionsmobilisierung, was anschließend von « Rauheitsmobilisierung » gefolgt wird. Das Letztere entspricht die Einleitung einer zunehmenden Abnahme des Porendruckes. Die Zu- und Abnahme des Porendruckes ist unterschiedlich zwischen Bausteine wegen des Einflusses der Rauheit der Bausteinsmorphologie. Das Streßverhalten für intakte Bausteine wird von den effektiven und augenblicklichen Druck, den differentiellen Streß und den maximalen induzierten Porendruck bestimmt, während es in klüftigen Bausteine von effektivene normalen Streß und Rauheitsmorphologie der Klüftflächen kontrolliert wird.

## 1 INTRODUCTION

The important role of pore pressure in hydromechanical stability of engineering works in rock masses (intact, jointed or faulted) was recognized since several decades (Lane 1970). However, few experimental studies of pore pressure effects on rock behavior are available in the literature (Aldrich 1969; Goodman & Ohnishi 1973; Mesri et al. 1976; Ismail & Murrell 1976). It was shown that for many porous rocks, the Terzaghi's effective stress law ( $\sigma' = \sigma - u$ ) was valid (Terzaghi 1945; Robinson 1959; Aldrich 1969). However, because of the great number of exceptions to the effective stress law observed in the case of rocks with low porosity and permeability, a more general equation ( $\sigma' = \sigma - \alpha \cdot u$ ) was developed by Skempton (1960) and reformulated by Nur & Byerlee (1971). The parameter  $\alpha = 1 - (K/K_s)$  is a function of the bulk moduli of the whole rock (K) and the grain ( $K_s$ ). Few experimental works were dedicated to pore pressure behavior and effects, under undrained conditions in rocks during their deformation, failure and post-failure phases (Aldrich 1969; Ismail & Murrell 1976); while Mesri et al. (1976) studied the pore pressure response in rock to undrained change in all-round or isotropic stress. Fewer studies were devoted to the same problem in jointed rock (Lane 1970; Goodman & Ohnishi 1973) but for smooth sawcut joints. No such studies were performed on rough irregular joints.

## 2 PORE PRESSURE BEHAVIOR IN UNDRAINED TESTS

Under undrained conditions, interstitial water is trapped within void spaces (pores and micro cracks) in the specimen. Dilatation

in the sample volume decreases the pore pressure, while contraction increases it. For this condition, it is assumed that water can move freely within the sample but not out of it. As a modification of the pore pressure changes the state of applied effective stress and consequently, the rock behavior; it is important to define the relation between the pore pressure variation resulting from a change in the state of applied stress. Skempton (1954) has developed such an empirical equation for soils in the following form :

$$u_i = B[\Delta\sigma_3 + A(\Delta\sigma_1 - \Delta\sigma_3)] = B \cdot \Delta\sigma_3 + \bar{A}(\Delta\sigma_1 - \Delta\sigma_3)$$

where  $\bar{A} = A \cdot B$ . The parameters B and A are respectively the induced pore pressure coefficients for a variation of the isotropic stress ( $\Delta\sigma_3$ ) and of the stress deviator ( $\Delta\sigma_1 - \Delta\sigma_3$ ). As the confining pressure stays constant during an undrained triaxial test ( $\Delta\sigma_3 = 0$ ), this study will evaluate the coefficient A only, related to the variation of the stress deviator ( $\Delta\sigma_1 - \Delta\sigma_3$ ).

### 2.1 Conditions of testing

An experimental verification of pore pressure behavior, under undrained conditions with intact and jointed specimens taken from a rock analog material, was performed through six series of triaxial shear tests under three different confining pressures ( $\sigma_3$ ) and three initial pore pressures ( $u_0$ ) for each  $\sigma_3$  value. The experimental program is detailed in Poirier et al. (1994). Profiles were taken on each fracture, around 10 for each surface tested, to characterize the fracture surfaces roughness. On the basis of the relationship between the  $Z_2$  statistical parameter of roughness and the JRC coefficient (Tse & Cruden 1979), JRC values were

computed for the nine fractures giving values between 7.2 and 8.9 with a mean around 8.

## 2.2 Induced pore pressure and $\bar{A}$ coefficient in relation with $(\sigma_1 - \sigma_3)$

Analyses of the pore pressure behavior in relation with stress-strain variation in intact and jointed specimens were detailed and illustrated in previous papers (Poirier et al. 1994; Archambault et al. 1998). Results indicate that the induced pore pressure ( $u_i$ ) response to an increase of the stress deviator  $(\sigma_1 - \sigma_3)$  follows the evolution of the volume of voids:  $u_i (= u - u_0)$ , where  $u$  is the instant pore pressure and  $u_0$  is the initial pore pressure). It increases non-linearly until unstable fractures propagate then decreases until  $u$  reaches zero (Fig. 1). But for high  $\sigma_3$  (13.8 MPa), the decrease of  $u$  stops before zero, because material plasticity condition is reached at this stress state. Higher values of  $u_{i\max}$  are reached for higher values of initial effective confining pressure  $(\sigma'_3)_0$  caused by the increasing failure strength and decreasing dilatancy. Figure 1 shows that within the same series of tests (same  $\sigma_3$ ) the linear portion of the curves to  $u_{i\max}$  are characterized by the same slopes,  $\bar{A} = \Delta u_i / \Delta(\sigma_1 - \sigma_3)$ . Also it can be observed that higher confining pressure  $(\sigma_3)$ , give higher pore pressure increasing rate. Induced pore pressure at failure is either negative or positive, depending on initial effective confining pressure  $(\sigma'_3)_0$  and it increases with increasing  $(\sigma'_3)_0$  so that a pressure threshold can be defined around  $(\sigma'_3)_0 \cong 9$  MPa.

Figure 2 shows the evolution of Skempton (1954) pore pressure coefficient  $\bar{A}$  ( $= \Delta u_i / \Delta \sigma_1$ , because  $\Delta \sigma_3 = 0$ ) with the variation of the stress deviator  $(\sigma_1 - \sigma_3)$ . Various initial effective confining pressure  $(\sigma'_3)_0$  influences the rate of variation of  $\bar{A}$  for an increase of  $(\sigma_1 - \sigma_3)$ . From these test results, it is noticed that for an initial effective confining pressure  $(\sigma'_3)_0 < 7$  MPa, the  $\bar{A}$  coefficient is approximately constant from the loading point to the initiation of dilatancy or  $u_{i\max}$  while  $\bar{A}$  increases gradually

for  $(\sigma'_3)_0 > 7$  MPa between the same limits. From the loading point to the dilatancy initiation phase the  $\bar{A}$  coefficient behavior is directly related to  $(\sigma'_3)_0$  and it may be stated that the higher the initial effective confining pressure  $(\sigma'_3)_0$  the higher the stress deviator  $(\sigma_1 - \sigma_3)$  must be to initiate dilatancy (Figs 1 and 2) or to reach  $u_{i\max}$  (or  $\bar{A} = 0$ ). After  $u_{i\max}$ , the results show that the pore pressure coefficient  $\bar{A}$  decreases rapidly, following an identical slope in all tests (Fig. 2), to reach a plateau at  $\bar{A} \cong -0.3$ . During this phase, it seems that  $(\sigma'_3)_0$  does not influence the  $\bar{A}$  coefficient behavior.

In the case of undrained triaxial shear tests on jointed specimens, induced pore pressure ( $u_i$ ) variation differs from one test to the other (Fig. 3). After  $u_{i\max}$ , the decrease in pore pressure differs in each test. Generally, the increase of pore pressure, the  $u_{i\max}$  value and the increasing rate of induced pore pressure ( $\Delta u_i / \Delta(\sigma_1 - \sigma_3) = \bar{A}$ ) are proportional to  $(\sigma'_3)_0$  like in the intact samples. Beyond  $u_{i\max}$ , the decrease in induced pore pressure is so irregular in each test and so different from one test to the other, that it is difficult to evaluate the influence of  $(\sigma'_3)_0$ . The increase and decrease in pore pressure ( $u$ ) and  $\bar{A}$  coefficient behave quite irregularly in each test and from test to test (Fig. 4) with an almost unpredictable evolution of pore pressure changing continually with the irregular dilatancy-contractancy behavior caused by the variable roughness morphology characterizing each fracture. Globally the values of  $\bar{A}$  varies from 0.01 to 0.3 and are proportional to the values of  $(\sigma'_3)_0$  varying from 0.3 to 4.1 MPa. They correspond to the increasing pore pressure during the friction mobilization phase with  $\bar{A}$  variations caused by the roughness morphology of the fractures. Mobilization of roughness and dilatancy with shear displacement, being dependent on roughness morphology on each fracture, show specific decreasing rate of pore pressure of the  $\bar{A}$  coefficient in relation with the dilatancy rate depending on the slip-shear processes on asperities of the fracture surfaces. Larger shear displacement, after peak shear strength, show large variation in the  $\bar{A}$  coefficient from positive to negative values with varying  $(\sigma_1 - \sigma_3)$ .

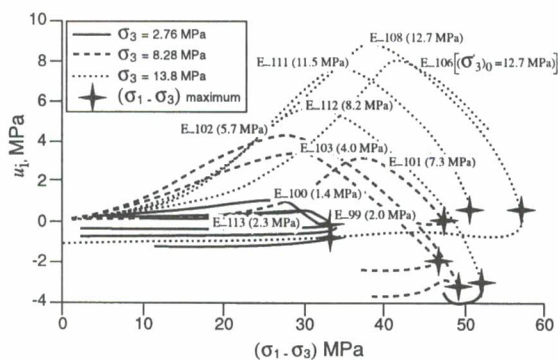


Figure 1. Induce pore pressure evolution with applied stress deviator on intact samples

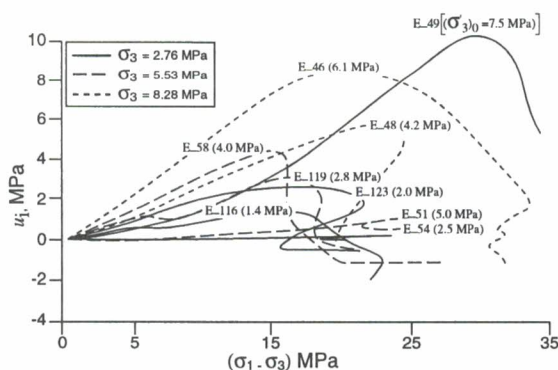


Figure 3. Induce pore pressure evolution with applied stress deviator on jointed samples

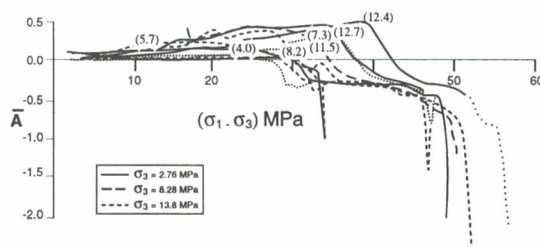


Figure 2. Evolution of the coefficient  $\bar{A}$  ( $\Delta u_i / \Delta(\sigma_1 - \sigma_3)$ ) with the stress deviator for the series of undrained triaxial tests on intact samples.

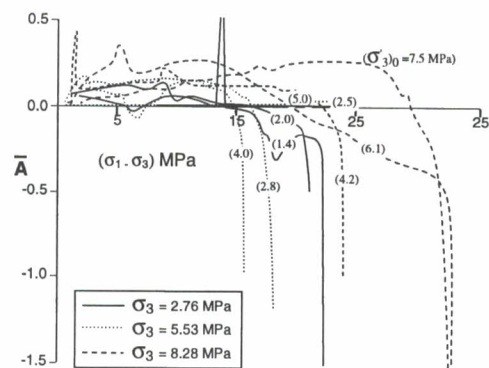


Figure 4. Evolution of the coefficient  $\bar{A}$  ( $\Delta u_i / \Delta(\sigma_1 - \sigma_3)$ ) with the stress deviator for the series of undrained triaxial tests on joint samples.

### 3 INDUCED PORE PRESSURE EFFECTS ON THE STRESS PATHS

The effective normal stress ( $\sigma'_n$ ) and the shear stress ( $\tau$ ) were computed from the effective principal stresses ( $\sigma'_1$  and  $\sigma'_3$ ) on each failure plane in intact and jointed specimens making an angle  $\theta$  between the normal to the plane and the specimen axis ( $\theta \cong 60^\circ$ ) and this from the loading point to post-failure deformation. On the basis of this computation, the stress paths of ( $\sigma'_n, \tau$ ) were determined and plotted in the Mohr diagrams (Figs 5 and 6) for drained and undrained conditions, giving linear and non-linear paths respectively.

The application of a stress deviator on a test specimen produces a volume reduction (contractancy) giving rise to an increase in pore pressure in two different phases. In the first phase, the pore pressure rise linearly till dilatancy initiates and the higher the initial effective confining pressure ( $\sigma'_3)_0$  is, higher the increasing rate of induced pore pressure [ $\Delta u_i / \Delta(\sigma_1 - \sigma_3)$ ] will be. Then the pore pressure increasing rate declines gradually to the maximum induced pore pressure ( $u_{i,max}$ ). This decreasing rate begins when the effective stress reached the dilatancy initiation threshold corresponding to the following limit:  $\sigma'_1 = 3.86 \sigma'_3 + 19.64$ , for this rock analog material. The unstable fracture propagation phase marked the beginning of pore pressure reduction caused by a dilatancy rate higher than the contractancy of pores and flaws within the material. This reduction in pore pressure induced a dilatancy hardening phenomenon increasing the material strength.

Figure 5 shows the stress paths followed during axial loading in comparison with the linear trajectories corresponding to drained test conditions on  $60^\circ$  inclined planes as mentioned earlier. The undrained stress paths show, before failure, a deviation from the drained paths caused by the induced pore pressure till dilatancy begins, then they follow the intact material Mohr failure envelope until peak shear strength is reached and finally fall progressively on the basic friction envelope, the two last phase corresponding to a decrease in pore pressure (Fig. 5). In fact, it can be observed from the undrained stress paths that pore pressure begins to decrease when the stress state in the specimens is quite near the Mohr failure envelope and from this point on, the decrease in pore pressure is such that dilatancy hardening prevent the occurrence of failure. If the pore pressure decrease is sufficient to insure the specimen stability, the stress path progresses tangentially to the Mohr failure envelope. These stress paths, evolving parallel to the failure envelope, explain why the decreasing rate of pore pressure is similar in all samples between the pore pressure reduction point and the failure point. It was

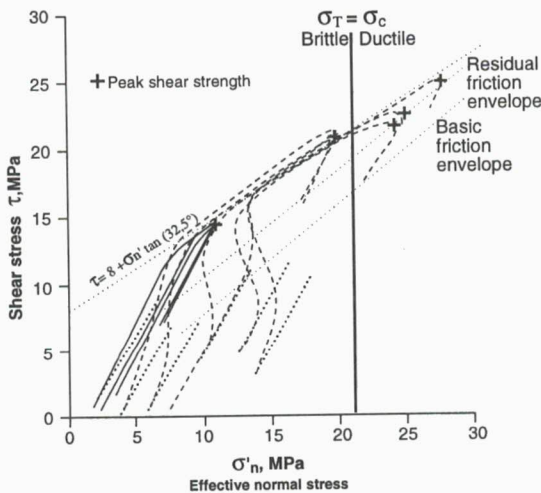


Figure 5. Stress paths in intact samples calculated with a hypothetical inclined plane at  $30^\circ$  with sample axis

noted that, just before failure, the decreasing rate of pore pressure seems to fall instantly and at this point, the dilatancy hardening being insufficient to insure sample cohesion, it fails. Then, the stress paths fall rapidly on the residual friction envelope.

In the case of the two first series of tests, pore pressure decreases very little after failure, not because of a lack of dilatancy, but because it is almost null and suction was not measured within the specimens. The consequence of this phenomenon is, for two samples submitted to the same initial effective confining pressure ( $\sigma'_3)_0$ , the shear strength in each sample depend on pore pressure. Higher shear strength corresponds to higher pore pressure and more important dilatancy hardening. The third series of tests show that dilatancy hardening does not extend necessarily to a null pore pressure, because in this series pore pressure is still positive after failure and this is caused by the stress state that has reached the material plastic behavior (Fig. 5). It can be stated that sample submitted to high pore pressure will not show a dilatancy hardening phase till pore pressure becomes null, but till plastic deformation is reached in which pore pressure variation becomes null.

Figure 6 shows that peak shear strength of jointed specimens is always well under the failure envelope of the intact material and depends essentially on the effective normal stress ( $\sigma'_n$ ). So, a variation in pore pressure affects the shear strength of the jointed specimens showing a dilatancy hardening with a decreasing pore pressure ( $u$ ) or a contractancy softening with an increasing pore pressure ( $u$ ). Observations of pore pressure variations from loading point to failure show positive induced pore pressure ( $u_i$ ) in all jointed specimens, except one (Fig. 3), giving rise to contractancy softening and a decreasing shear strength of the undrained rough joints relatively to the drained ones. But, just before and at peak shear strength, there was a significant decrease in pore pressure (Fig. 3) resulting in an increasing effective normal stress ( $\sigma'_n$ ) and peak shear strength. This

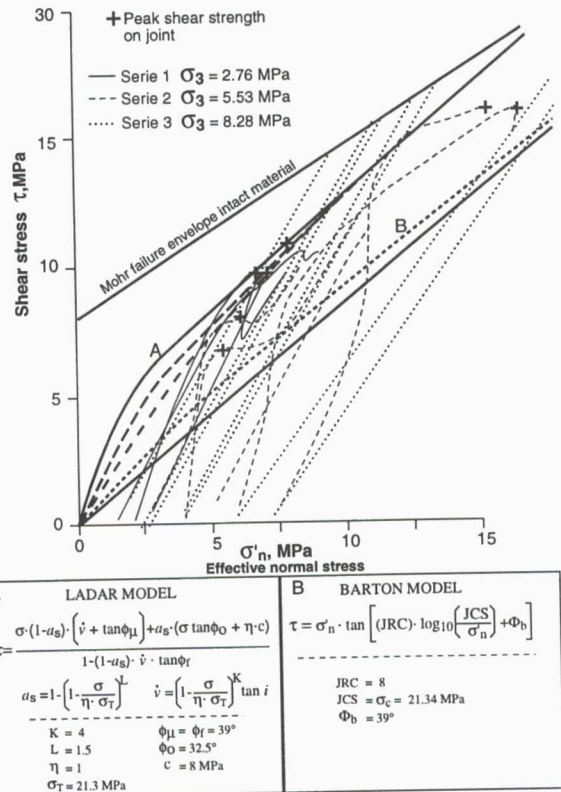


Figure 6. Stress paths in the jointed samples with comparison of joint shear strength results with LADAR model for values of  $i = 20^\circ, 30^\circ, 40^\circ$  and Barton's model for a  $JRC = 8$

situation is well demonstrated by the undrained stress paths (Fig. 6), relatively to the corresponding drained ones, in which the effective normal stress ( $\sigma'_n$ ) increase rapidly before peak shear strength. Contrary to intact specimens, the exact causes of pore pressure variations within jointed specimens are difficult to evaluate, because the effective confining pressure ( $\sigma'_3$ ) is not the only determinant factor to intervene; the roughness morphology of the joint surfaces plays a major role on pore pressure evolution.

During the friction mobilization phase, all the tests show an increasing pore pressure with the increasing deviatoric stress ( $\sigma_1 - \sigma_3$ ) caused by a reduction in volume (contractancy) within the intact material and reduction of the aperture between the joint surfaces. It is impossible to differentiate between the increase of pore pressure caused by both phenomena. Nevertheless, for the same initial effective confining pressure in both types of specimens (Figs 5 and 6) the increase in pore pressure in the jointed specimens is higher than in the intact ones (Figs 1 and 3). In spite of the numerous fluctuations, higher initial effective confining pressure ( $\sigma'_3)_0$  caused higher pore pressure increasing rate with increasing differential stress ( $\sigma_1 - \sigma_3$ ) (Fig. 4). Pore overpressure in jointed specimens is caused by increasing normal stress on the joint inducing a closure of the aperture between the joint walls and restraining dilatancy between them. This phenomenon is characterized by an increasing slope deviation in the stress path with increasing confining pressure ( $\sigma_3$ ) (Fig. 6). The more important morphologic characteristics of the surfaces responsible for this phenomenon are most probably the degree of interlocking and the contact areas between the joint surfaces which depend on the roughness morphology and applied normal stress. Roughness morphology of the joint surfaces is also responsible of induced pore pressure fluctuations during the roughness mobilization (dilatancy) phase. Episodic local slips on asperity surfaces create instant dilatancy and pore pressure decrease slightly at this moment (Fig. 4). This phenomenon is more frequent in the case of low normal stress and low asperities slopes (i).

Figure 6 shows also the undrained triaxial shear test results of jointed specimens in relation with LADAR model (Ladanyi and Archambault 1970) for angles of asperities  $i = 20^\circ, 30^\circ$  and  $40^\circ$  and Barton's model (Barton 1973) for a  $JRC \cong 8$  determined previously. Parameters conditions and models equations are given in Figure 6. A slightly better agreement between LADAR model and test results can be noticed with low normal stress while Barton's model underestimates slightly peak shear strength of joints, but gives strength values on the safe side. Overall test results are in fact between both models theoretical shear strength behavior. Two of the specimens show a stress path different from others with a large increase in effective normal stress ( $\sigma'_n$ ) caused by dilatancy hardening resulting from a rapid decrease in pore pressure before failure.

#### 4 CONCEPTUAL MODELLING

Figure 7 shows schematic representation of stress paths evolution in undrained tests mobilizing both brittle and plastic behavior. The first stress path illustrated is for triaxial shear test under initial effective normal stress  $(\sigma'_n)_0$  between 0 and  $0.5 \sigma_T$  (point A), corresponding to the two first series of tests. The application of a differential stress ( $\sigma_1 - \sigma_3$ ) increases the pore pressure gradually to unstable fracture propagation point B for a stress level slightly under the intact material failure envelope. This increase in pore pressure causes a deviation in the stress path with a slope higher than the  $60^\circ$  path of drained conditions. So, the higher the initial effective confining pressure  $(\sigma'_3)_0$  the larger the deviation from the  $60^\circ$  drained stress path. Then, a decrease in pore pressure causing a new deviation in the stress path with a slope less than  $60^\circ$  brings the stress state on the failure envelope. Despite this fact, dilatancy hardening prevents the sample failure and the stress path displaced itself along the

failure envelope till pore pressure  $u \cong 0$  or till the decreasing rate of pore pressure is insufficient to prevent failure.

As the effective stress law can be applied to the rock analog material, specimens with the same initial effective normal stress, but for different initial stress, will fail at different positions on the failure envelope. In fact, as induced pore pressure ( $u_i$ ) will be the same for all specimens, the higher the initial pore pressure ( $u_0$ ) will be, the higher the resulting maximum pore pressure ( $u_{max} = u_0 + u_i$ ) will reach and there will be a necessary increase in dilatancy to reach a null pore pressure ( $u \cong 0$ ). So, this increase in dilatancy is possible only through a stress path along the failure envelope (points C and E). Then, the stresses ( $\tau, \sigma'_n$ ) decrease on a  $60^\circ$  drained stress path to reach the residual friction envelope (points D and F). Sometimes, pore pressure ( $u$ ) can be different from 0 at failure and pore pressure decreases beyond failure and the stress path is inclined over  $60^\circ$  as shown in inset (Fig. 7).

When the necessary dilatancy to obtain  $u \cong 0$  is too high the stress path reach the plastic limit. At the brittle-ductile transition zone, the stress path deviates towards the residual friction envelope. At this point, the dilatancy rate is almost null [ $\Delta u_i / \Delta(\sigma_1 - \sigma_3) \cong 0$ ] and there is no more dilatancy hardening in this phase. The specimen has reached maximum strength (point G) and the stress state decrease to stabilize itself between residual and basic friction envelopes (point H). As the stress state is still decreasing instead of stabilizing at point G, it is not characterized by perfect plasticity but is localized within the brittle-ductile transition zone (the limit  $\sigma_T = \sigma_c$  being an approximate limit criteria). The second stress path (Fig. 7) illustrates the conditions for which the initial effective normal stress  $(\sigma'_n)_0 > 0.5 \sigma_T$ . In this initial stress state, the maximum pore pressure ( $u_{max}$ ) reached, prevent brittle failure and forces the stress path through the brittle-ductile zone. When pore pressure ( $u$ ) increases, the stress path deviation is larger than for  $(\sigma'_n)_0 < 0.5 \sigma_T$  and its slope is also greater and its rate increases progressively. When pore pressure ( $u$ ) decreases (point J), the stress path follows the points E, G and H and the processus of evolution is as described previously.

Figure 8 shows the schematic stress path of a jointed specimen. The A-B segment of the stress path correspond to the friction mobilization phase in which pore pressure increase is due to the intact material contractancy and aperture closure between the joint walls. In the intact material, the higher the initial stress state, the more rapid is the increasing rate in pore pressure or slope of the stress path which depends also on the degree of porosity. Within the joint, high stress state reduces the induced pore pressure caused by the decreasing compressibility with increasing stress level, so the slope of the stress path is also reduced with an increasing stress level. Joint roughness morphology plays an important role on joint compressibility, so that high roughness induced larger compressibility, and the slope of the stress path increase, but this effect is reduced with increasing initial stress level. The stress path is not always linear because of adjustments on rough surfaces.

During the roughness mobilization phase, the undrained triaxial shear tests show decreasing pore pressure caused by dilatancy within the joint with slips on asperities slopes. Dilatancy is controlled by angularity distribution of asperities and normal stress level applied on the rough joint plane and so for the decreasing pore pressure ( $u$ ). Observations of the stress paths (Fig. 6) in the roughness mobilization phase shows that they are different in each test. As pore pressure decrease is caused by dilatancy, the stress path is controlled by the joint roughness morphology. So, high dilatancy rate mobilization (meaning high angularity of asperities) increases the normal stress with decreasing pore pressure and reduces the slope of the stress path. But as there is no direct relation between the volume variation of voids and dilatancy, it is difficult to give an interpretation of the stress paths. The segment B-C of a jointed specimen schematic stress path (Fig. 8) shows that the beginning of the roughness mobilization phase is characterized by a stress path slope inferior to the drained one. The slope of the stress path depends on the

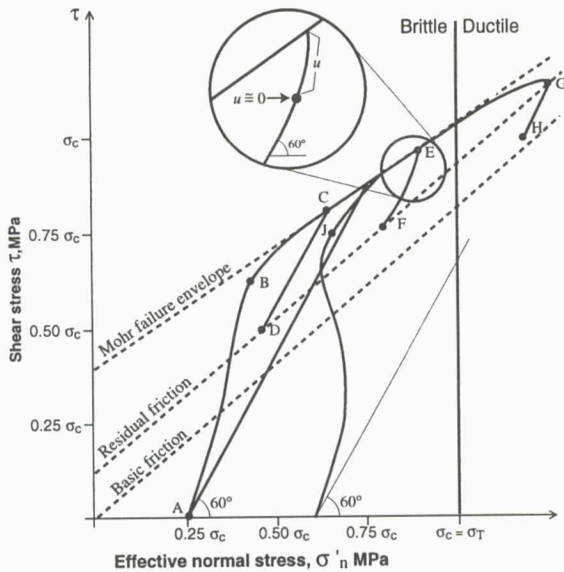


Figure 7. Conceptual modeling of stress path evolution in undrained intact samples

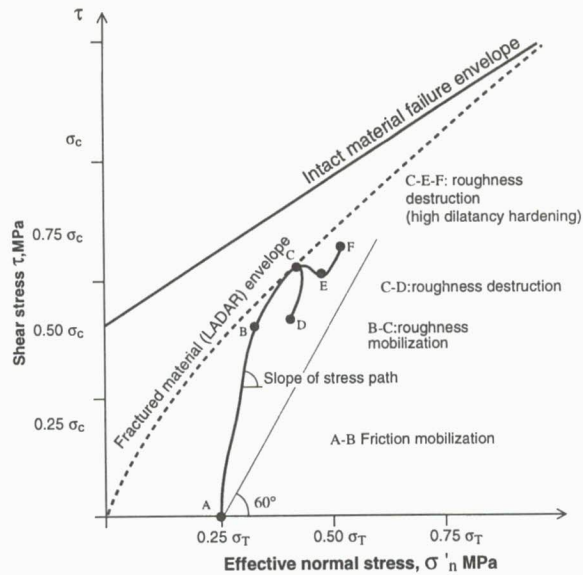


Figure 8. Conceptual modeling of stress path evolution in undrained jointed samples

roughness morphology and the applied stress state but this relationship is still to be defined. This phase ends when the effective stresses reached the joint peak shear strength. LADAR model was chosen in this case because it gives an adequate failure criteria for the jointed material tested. Between the beginning and end of the roughness mobilization phase, the slope of the stress path, can vary with adjustments between the joint rough surfaces during shear displacement.

During the roughness destruction phase, after peak shear strength, all the tests show a reduction in pore pressure and slips occur on roughness asperities that are gradually sheared off with the increasing stress state on the joint surfaces. This phenomenon caused a reduction in the mobilized angularity and by consequence the dilatancy becoming null at certain point. Progressively, the slope of the stress path becomes parallel to the drained one (Fig. 6) and it happens sometimes that dilatancy hardening is such that it raises the stress state. The schematic stress path (Fig. 8) in the roughness destruction phase show that, depending on dilatancy hardening, its slope tends towards the drained one (C-D segment). Because of important dilatancy hardening and the triaxial loading state of the jointed specimen, sometimes an increasing stress state occurred. When this phenomenon happened, the stress path is parallel to drained conditions with increasing stresses (C-E-F segment).

## 5 CONCLUSION

The maximum induced pore pressure, in intact specimens, is a function of the confining pressure, initial pore pressure and volumetric strain. In jointed samples, the controlling factors were the effective normal stress and the morphology on the joint surfaces. Stress paths in both type of samples show an important dilatancy hardening phenomenon before peak shear strength. In both cases, the higher the initial pore pressure and effective confining pressure, the larger is the deviation in the stress paths from the drained stress paths. The jointed samples show more irregular stress paths in relation with their roughness morphology.

## REFERENCES

Aldrich, M.J. 1969. Pore pressure effects on Berea sandstone subjected to experimental deformation. *Geol. Soc. Am. Bull.*, 80 : 1577-1586.  
 Archambault, G., Poirier, S., Rouleau, A., Gentier, S. & Riss, J. 1998. The behavior of induced pore fluid pressure in undrained triaxial

shear tests on fracture porous analog rock material specimens. *Mechanics of Jointed and Faulted Rock*, Rossmanith (ed.), Balkema, pp. 583-589.  
 Barton, N.R. 1973. Review of a new shear strength criterion for rock joints. *Engineering Geology*, 7 : 287-332.  
 Goodman, R.E. & Ohnishi, Y. 1973. Undrained shear testing of jointed rock. *Rock Mechanics*, 5 : 129-149.  
 Ismail, I.A.H & Murrell, S.A.F. 1976. Dilatancy and the strength of rocks containing pore water under undrained conditions. *Geophys. J. R. Astr. Soc.*, 44 : 107-134.  
 Ladanyi, B. & Archambault, G. 1970. Simulation of Shear Behavior of a Jointed Rock Mass. *Rock Mechanics*, W.H. Somerton (ed.), American Institute of Mining, Metallurgical, and Petroleum Engineers, New York, pp. 105-125.  
 Lane, K.S. 1970. Engineering problems due to fluid pressure in rock. *Rock Mechanics - Theory and Practice*. W.H. Somerton. American Institute of Mining, Metallurgical, and Petroleum Engineers, New York, pp. 501-540.  
 Mesri, G.K., Adachi & Ullrich, C.R. 1976. Pore pressure response in rock to undrained change in all round stress. *Geotechnique*, 26 (2) : 317-330.  
 Nur, A. & Byerlee, J.D. 1971. An exact effective stress law for elastic deformation of rock with fluids. *JGR*, 76 (26) : 6414-6419.  
 Poirier, S., Archambault, G. & Rouleau, A. 1994. Experimental Testing of Pore Water Influences on Physico-Mechanical Properties of a Porous Rock Analog Material. In *Proc. of 47<sup>th</sup> Canadian Geotechnical Conf.*, Halifax, NS, pp. 418-427.  
 Robinson, L.H. 1959. The effect of pore and confining pressure on the failure process in sedimentary rock. *3<sup>rd</sup> Symp. Rock Mech. Quart. Colo. School Min.*, 54 : 177-199.  
 Skempton, A.W. 1954. The pore pressure coefficient A and B. *Geotechnique*, 4 : 143-147.  
 Skempton, A.W. 1960. Effective stress on soil, concrete and rock in pore pressure and suction in soils. *Butterworths, London*, 4-16.  
 Terzaghi, K. 1945. Stress conditions for the failure of saturated concrete and rock. *Compte rendu de l'ASTM*, 45 : 777-792.  
 Tse, R. & Cruden, D.M. 1979. Estimating joint roughness coefficients. *Int. J. Rock Mech. Min. Sci. and Geomech. Abstracts*, 16 : 303-307.